Soft Matter

ROYAL SOCIETY OF CHEMISTRY

PAPER

Published on 01 June 2026

Cite this: *Soft Matter*, 2026, **22**, 4784

Dynamics of weakly magnetic nanoparticle suspensions near a magnetized sphere

Mohd Bilal Khan,[ab] Abigail Patterson,[ab] Jamel Ali,[ab] Theo Siegrist,[ab] Munir Humayun[ac] and Hadi Mohammadigoushki *[ab]

We report experimental and multiphysics simulation studies of magnetophoretic transport and capture of nanoparticles around a magnetized sphere under high-gradient magnetic fields. Experiments were performed using a broad range of paramagnetic and diamagnetic nanoparticles at an imposed magnetic field up to $\mathbf{B}_0$ = 1 T and concentrations of c_0 = 10–100 mg L^{-1}. Paramagnetic nanoparticles exhibited substantially enhanced capture compared to diamagnetic nanoparticles, with capture efficiency increasing nonlinearly with magnetic field strength, initial nanoparticle concentration, and magnetic susceptibility. In addition, increasing the sphere diameter also improved the capture efficiency of paramagnetic nanoparticles despite reducing local magnetic field gradients. Our analysis showed that the observed rate of nanoparticle capture by the non-uniform magnetic-field exceeded predictions from a simple scaling analysis and isolated-particle magnetophoresis. More detailed analysis using multiphysics numerical simulations suggests magnetic field-induced nanoparticle clustering, which in turn significantly enhances the transport of nanoparticles. In addition, field-induced convective flows were found to substantially promote nanoparticle transport. These results highlight that magnetophoretic capture of weakly paramagnetic materials in high-gradient magnetic systems is governed by a nonlinear coupling of magnetic and flow-driven transport mechanisms. These results provide insights into the design of magnetic separation systems for recovery and recycling of weakly magnetic nanoparticles and colloidal suspensions.

Received 27th March 2026,
Accepted 28th May 2026

DOI: 10.1039/d6sm00260a

rsc.li/soft-matter-journal

1 Introduction

The selective capture of nanoparticles in suspension underpins a broad range of technologies, including water treatment,[1] mineral processing,[2] biomedical imaging,[3] resource recovery,[4] and targeted therapies.[5] In particular, the recovery of critical metals from end-of-life electronics, batteries, and permanent magnets, as well as the purification of industrial effluents, increasingly requires the separation of weakly paramagnetic and diamagnetic nanoparticles.[6–11] Conventional separation methods such as filtration, centrifugation, and sedimentation are often ineffective at the nanoscale due to the particles' negligible inertia, strong Brownian agitation, and potential chemical or environmental hazards.[12–15] Magnetically assisted separation has therefore emerged as a non-invasive and energy-efficient alternative for isolating weakly magnetic nanoparticles.[16,17]

Magnetophoresis, the underlying physical principle for magnetically assisted separation, exploits differences in magnetic susceptibility in the presence of strong magnetic-field gradients. Nanoparticles with positive magnetic susceptibility (paramagnetic) are drawn toward regions of high field intensity. In contrast, particles with negative susceptibility (diamagnetic) experience a repulsive force and thus exhibit little or no retention under comparable conditions.[18]

The study of magnetophoresis spans more than five decades and encompasses a broad spectrum of particle types, magnetic field strengths, and separation architectures.[18] Two distinct regimes dominate the literature, high-gradient magnetic separation (HGMS), which employs ferromagnetic matrices that generate an extremely strong local field to capture strongly magnetic particles, and low-gradient magnetic separation (LGMS), which exploits weaker fields yet can yield unexpectedly rapid removal of superparamagnetic nanoparticles.[19] Classical HGMS focuses on micron- and nanometer-scale particles with relatively large magnetic susceptibilities.[20–26] In contrast, LGMS typically operates with much weaker gradients yet has been shown to remove superparamagnetic nanoparticles at rates far exceeding those predicted by single-particle magnetophoretic theory.[19,27–31] Early experimental work revealed removal

[a] *Department of Chemical and Biomedical Engineering, Florida State University, Tallahassee, Florida-32310, USA. E-mail: hadi.moham@eng.famu.fsu.edu*
[b] *Center for Rare Earths, Critical Minerals, and Industrial Byproducts, National High Magnetic Field Laboratory, Tallahassee, FL 32310, USA*
[c] *Department of Earth, Ocean and Atmospheric Science, Florida State University, Tallahassee, FL 32304, USA*

efficiencies far higher than expected for isolated nanoparticles migrating through quiescent fluids.[19] This discrepancy led to the hypothesis that applied magnetic fields induce reversible nanoparticle clustering, which may in turn create larger, and more magnetically responsive aggregates that experience substantially greater magnetophoretic forces.[32–39]

Despite significant advances in both HGMS and LGMS, particularly for superparamagnetic iron-oxide nanoparticles and microparticles, a substantial gap remains in understanding magnetophoresis of weakly paramagnetic and diamagnetic nanoparticles that are relevant to the critical materials found in electronic waste (*e.g.*, nickel, cobalt, manganese, bismuth, zinc, among others). As the volume of spent electronic waste continues to grow, recovering and reusing these critical metals has become increasingly important for reducing dependence on natural resources, strengthening supply chains, and mitigating environmental impacts.[40,41] These species have magnetic susceptibilities orders of magnitude smaller than those of superparamagnetic systems, placing them in a regime where magnetophoretic transport competes strongly with Brownian diffusion.[29] Recent work indicates that, beyond field-induced clustering observed in super paramagnetic nanoparticle suspensions, weakly magnetic nanoparticles may also experience field-driven convective flows that enhance their transport and separation.[42,43] Furthermore, the field-induced convective flows could be substantially amplified in the vicinity of magnetized ferromagnetic wires.[43]

Although spherical ferromagnetic collectors have been shown to efficiently capture superparamagnetic nanoparticles,[44–46] the magnetophoretic transport of weakly magnetic nanoparticles near a magnetized sphere remains comparatively underexplored. Most prior studies have focused on superparamagnetic particles, whose large magnetic susceptibilities produce strong magnetophoretic forces and rapid capture. In contrast, weakly paramagnetic and diamagnetic nanoparticles require substantially higher magnetic field gradients for effective manipulation. Moreover, the coupled effects of nanoparticle magnetic susceptibility, initial concentration, and applied magnetic field strength on the capture efficiency of weakly paramagnetic and diamagnetic particles have not been systematically investigated. The roles of field-induced particle clustering, and magnetically driven convective flows near magnetized ferromagnetic collectors also remain poorly understood, which makes it unclear whether such mechanisms established for superparamagnetic particles can be leveraged for the separation of weakly paramagnetic or diamagnetic nanoparticles. In summary, the transport behavior of weakly magnetic nanoparticles in localized high-gradient magnetic fields remains poorly understood, and coupled experimental and multiphysics numerical simulations are needed to enable a more in-depth understanding of the mechanisms involved in magnetophoresis of these systems.

The main goal of this study is to provide an in-depth analysis of magnetophoretic motion of weakly paramagnetic and diamagnetic nanoparticles under a high gradient magnetic field. To accomplish this goal, we will investigate the magnetophoresis dynamics of a diverse set of weakly paramagnetic (Mn_2O_3, Co_2O_3, Fe_2O_3, CuO) and diamagnetic (Bi_2O_3, ZnO) nanoparticles in the vicinity of a magnetized stainless-steel sphere. These metal oxides are commonly found in spent batteries and other electronic waste components such as cathode/anode materials, protective casings, and PCBs.[47,48] We will perform systematic experiments over a broad range of initial concentrations, imposed magnetic fields, and magnetic susceptibilities. The experimental measurements are complemented by three-dimensional multiphysics numerical simulations, which in turn enable detailed analysis of field-induced cluster formation, field-driven convective flows, and flow structures around the magnetized sphere.

2 Experiments

2.1 Materials

Paramagnetic and diamagnetic nanoparticles with various magnetic susceptibilities were obtained from Sigma-Aldrich and used as received. Their magnetic susceptibility values and vendor provided sizes are presented in Table 1.

In addition, polyethylene glycol (M = 6000 [$g\ mol^{-1}$]) was obtained from Sigma Aldrich and used as received. The nanoparticle suspensions are prepared using deionized water. Due to their strong magnetic properties, three different stainless steel spheres; 420 and 440 grade (provided by Bal-tec), and 430 grade (provided by Global Precision Ball) were used in the experiments. The radius of the spheres varied from 2 to 5 mm within a standard-size cuvette made up of polystyrene (12.5 mm × 12.5 mm × 45 mm).

2.2 Solution preparation

To improve particle stability and prevent aggregation in solution, we functionalize the surface of nanoparticles with polyethylene glycol (PEG), a widely established approach.[14] PEG is added at a concentration ten times higher than that of the nanoparticles, followed by a 1 hour incubation to ensure complete dispersion in deionized water. Afterward, the solution was homogenized using a vortex mixer. To further reduce the risk of aggregation, the solution was sonicated for 30 minutes in a bath sonicator to effectively disrupt any potential aggregates and promote uniform dispersion.

2.3 Magnetophoresis setup

The experimental setup for the magnetophoresis studies comprises several key components as illustrated in Fig. 1. A 1 T

Table 1 A summary of nanoparticles used in this study along with their most relevant properties

Type	Particle	$\Delta\chi_v$[49]	Radius[a] [nm]
Paramagnetic	Mn_2O_3	5.61×10^{-3}	50
	Fe_2O_3	5.05×10^{-3}	30
	Co_2O_3	2.91×10^{-3}	50
	CuO	2.46×10^{-4}	40
Diamagnetic	Bi_2O_3	-1.81×10^{-5}	40
	ZnO	-1.45×10^{-5}	18

[a] Specified by vendor. Here $\Delta\chi_v = \chi_v|_{particle} - \chi_v|_{water}$.

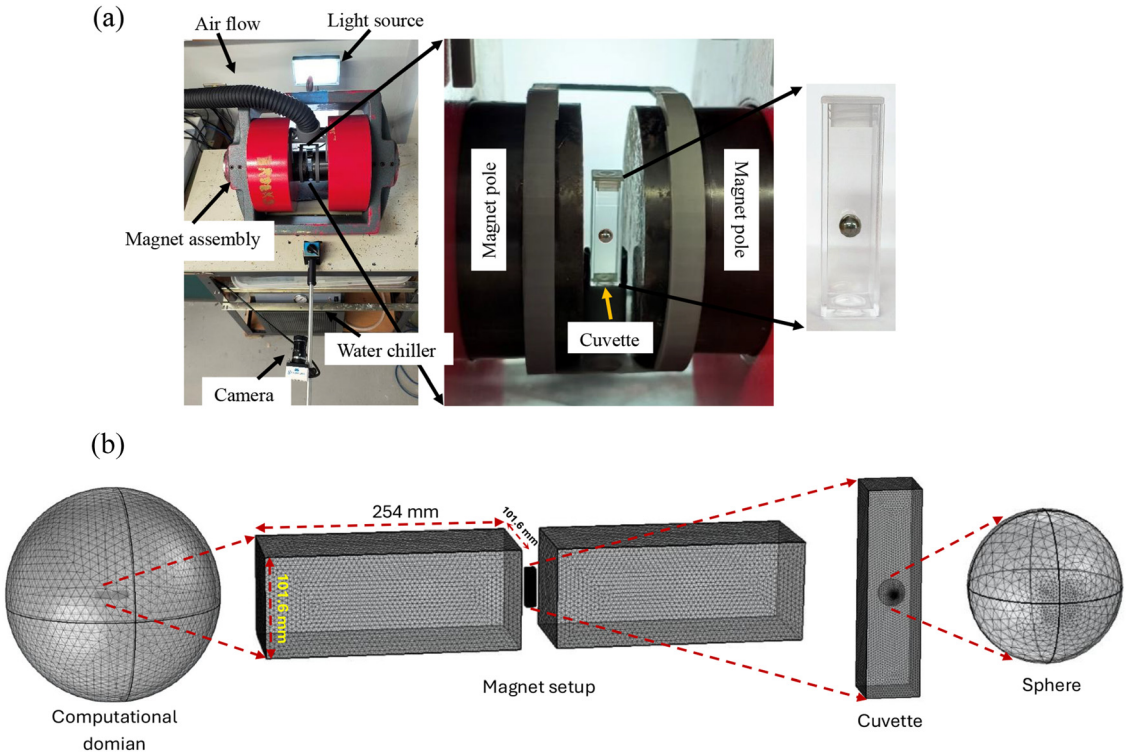

Fig. 1 (a) The top view of the experimental setup consisting of the camera, light source, electromagnet and the temperature controller. A closer view of the cuvette placed between the two flat poles is also presented in this section. (b) The computational domain along with the mesh density used for the present study.

electromagnet with pole diameters of 10 cm is used to generate the magnetic field. A ferromagnetic sphere is centrally positioned within a cuvette, and the applied magnetic field is horizontal between the two pole pieces. The sphere is attached to a wall of the cuvette using glue. A high-resolution camera is mounted to capture detailed images of nanoparticle dispersion around the sphere and within the surrounding fluid domain. Another method for generating localized magnetic field gradients is the use of spherical NdFeB permanent magnets. However, our calculations show that the field gradients around spherical permanent magnets are significantly smaller than those produced around a magnetized stainless-steel sphere inside an electromagnet, resulting in weaker magnetophoretic forces on weakly magnetic nanoparticles (see more details below and later in Fig. S1 of the SI). Perhaps more importantly, permanent magnets present important experimental limitations because they are always active. As soon as the suspension is introduced into the cuvette, particle migration begins, making it difficult to establish reproducible initial conditions. In contrast, the electromagnet-based setup allows the suspension to rest before the field is applied, minimizing residual convective flows and enabling experiments to start from well-defined quiescent conditions.

2.4 Particle concentration evaluation

To assess the spatio-temporal evolution of nanoparticle concentration throughout the cuvette, we first measure the averaged light absorbance of the solution within the cuvette at various initial concentrations ranging from 10 to 100 mg L^{-1}. As shown in Fig. S2 of the SI, the averaged normalized absorbance intensity within the cuvette increases linearly with initial concentration indicating that the Beer–Lambert law[50,51] is valid (see the SI for further discussion on the calibration curves).

2.5 Magnetization curve measurement

The magnetization curve of the stainless steel spheres was measured using a vibrating sample magnetometer (VSM) option for the Physical Property Measurement System (PPMS, Quantum Design) at the National High Magnetic Field Laboratory. The sphere was securely mounted on a brass trough holder using GE-7031 varnish. During the measurements, the vibration frequency was maintained at 40 Hz, while the amplitude was adjusted between 0.2 mm and 2 mm to optimize the signal strength.

3 Multiphysics numerical simulations

In addition to the detailed experiments, we performed comprehensive multiphysics numerical simulations. The coupled problem involves solving three key governing equations; static magnetic field, momentum, and mass balance, which are discussed in detail in our previous publications,[42,43] and are not presented in the main body of text for brevity but a summary of those systems of equations is provided in Section SII of the SI.

The simulations were conducted in three dimensions (3D) to capture the full geometry and physics of the experimental setup. As shown in Fig. 1(b), the 3D computational domain consists of a cuvette with dimensions identical to those used in the experiments. The magnetic pole pieces were modeled as rectangular prisms with dimensions specified in Fig. 1(b), separated by a 12.7 mm gap consistent with the experimental configuration. Although in our previous work,[42] we demonstrated that the electromagnet can be accurately represented in a two-dimensional axisymmetry, an axisymmetric simplification is not feasible in this study due to the misalignment between the electromagnet and the cuvette axis of symmetry and the fact that the bottom and the top of the sphere show different magnetophoretic dynamics. Therefore, the pole pieces were approximated as rectangular prisms. To ensure that the resulting magnetic field matched that of the experimental electromagnet, the size of the permanent magnets was adjusted to generate a uniform magnetic field of 1 T around the cuvette (see below).

The multiphysics numerical simulations were carried out using the finite element method-based COMSOL Multiphysics 6.1. The computational domain, which includes the surrounding environment with a radius of 2 m, was discretized into 31 098 elements, of which 30 089 were tetrahedral meshes. The batch vessel was resolved using 554 651 elements with a maximum mesh size of 0.5 mm. To optimize computational performance, the mesh size progressively increases with a maximum element growth rate of 1.15.

4 Results and discussion

Before conducting experiments involving magnetic fields and nanoparticle transport, we first performed a detailed characterization of the sedimentation dynamics of the nanoparticles. Such measurements allow us to accurately assess the polydispersity of the nanoparticle suspension. The experimental measurements, presented in the SI, were quantitatively compared with numerical simulations and showed excellent agreement. The results indicate that while most particles conform to the vendor-specified size, a small fraction tends to form weak aggregates even in the absence of a magnetic field. To capture this polydispersity, the particle size distribution was modeled as $\sum_{i=1}^{3} \phi_i R_{\mathrm{pi}}$, where ϕ_i and R_{pi} represent the volume fraction and radius of the i-th particle class, respectively. The fitted parameters and associated data are summarized in Fig. S3 and Table SI of the SI. In addition, to assess the particle size distributions in these suspensions, we performed dynamic light scattering (DLS) experiments. However, DLS is most sensitive to larger particles, and even a small number of larger particles can strongly bias the measured distribution and increase the particle size distribution. Consequently, even a relatively small population of larger particles or aggregates can disproportionately bias the measured size distribution and artificially increase the apparent polydispersity. This limitation is particularly important for the present suspensions, where broad particle size distributions may be present. This will make DLS less reliable for accurately resolving the underlying primary particle size distribution. The measured hydrodynamic sizes and polydispersity indices are reported in Table SII of the SI. In contrast, the particle size distributions obtained from the multiphysics simulations, which include a long tail extending toward particle sizes of approximately 150–200 nm, provide substantially better agreement with the experimentally observed sedimentation dynamics. These inferred distributions are also generally smaller than the DLS-derived hydrodynamic sizes, which is consistent with the known tendency of DLS to overemphasize larger particles. Therefore, throughout the remainder of this manuscript, we use the particle size distributions obtained by matching the sedimentation experiments with the numerical simulations as a benchmark to compare with those particle size distributions obtained under a magnetic field.

4.1 Static magnetic field

Any magnetophoresis simulation first requires the computation of the static magnetic field, which subsequently serves as an input to the mass transport and momentum equations. Therefore, we first evaluate the spatial distribution of the magnetic field around a magnetizable sphere. Fig. 2(a) and (b) present the calculated magnetic flux density, $\mathbf{B}$, and its gradient, $(\mathbf{B}\cdot\nabla)\mathbf{B}$, in the vicinity of a 5 mm stainless steel (type 430) sphere. When the external magnetic field lines intersect the sphere, the material becomes magnetized, and produces a localized enhancement in the magnetic field and a strong non-uniform field gradient. The resulting field gradient is predominantly positive near the lateral flanks of the sphere and negative along its polar regions (top and bottom). In these simulations, the experimentally measured M–H magnetization curve for the stainless steel sphere (as shown in Fig. 2(c)) was incorporated. The magnetic field in the vicinity of the sphere cannot be measured accurately due to spatial resolution limits and field perturbations near the metal surface. Therefore, to validate the numerical model, the computed magnetic field and its gradients were compared with the corresponding analytical closed-form solution.[52] Fig. 2(d) and (e) show a comparison between the numerically calculated magnetic field and magnetic field gradients around the sphere and those predicted analytically. The result shows excellent agreement between the numerical results and analytical predictions, which confirm the accuracy of the magnetic field computations used in subsequent transport simulations. Since the cuvette walls are composed of non-magnetic material, they do not generate localized magnetic field gradients capable of inducing nanoparticle accumulation. As shown in the above, the externally applied magnetic field remains approximately uniform close to the cuvette walls.

4.2 Magnetophoretic dynamics

4.2.1 Impact of sphere magnetization. Fig. 3 shows the spatiotemporal evolution of particle concentration in paramagnetic manganese oxide and diamagnetic bismuth oxide

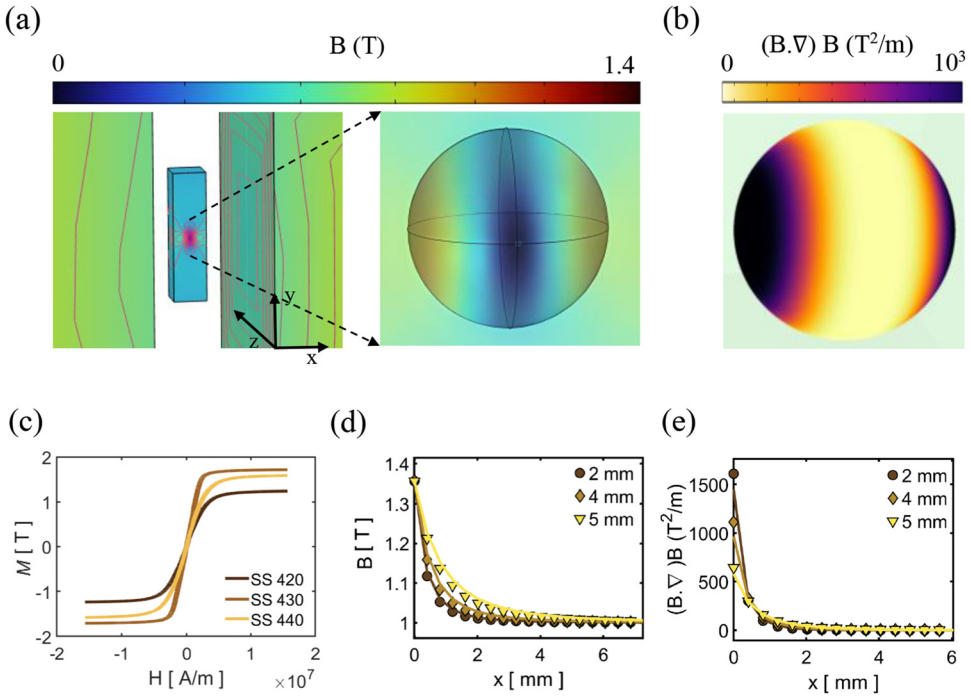

Fig. 2 Three-dimensional simulation of the magnetic flux density (a), and magnetic flux density gradients (b) around a sphere with a diameter of 5 mm under the influence of B_0 = 1 T applied magnetic field. The magnetic field is applied in the x-direction. (c) The measured M–H curves for three different grades of stainless steel spheres (420, 430 and 440). (d) Averaged magnetic flux density and (e) its gradients around spheres of different diameters under conditions of B_0 = 1 T. Here, symbols represent the simulation results, while curves show theoretical predictions, where x = 0 corresponds to the sphere surface.

nanoparticle suspensions at an initial concentration of c_0 = 100 mg L^{-1}, and an imposed magnetic flux density of $\mathbf{B}_0$ = 1 T for various stainless steel spheres. Fig. 3(a) shows the spatio-temporal evolution of particle concentration in experiments and simulations for the paramagnetic Mn_2O_3 nanoparticle solution. After applying the magnetic field, the particles start migrating towards the magnetized region of the sphere where the magnetic gradient is high. This particle migration initiates a transfer of momentum to the fluid, giving rise to upward fluid motion in the wake of the sphere (see also Movie S1 in the SI). As nanoparticles accumulate near the sphere surface, the adjacent fluid becomes increasingly depleted, resulting in localized density, and magnetic susceptibility gradients around the sphere. This imbalance generates a convective force that further drives upward flow, reinforcing the convective motion initiated by particle migration.[53,54] Over time, particle movement and induced fluid motion enhance transport efficiency and lead to significant particle accumulation around the sphere. As a result, the bulk concentration of the nanoparticles within the cuvette starts to decrease.

Fig. 3(c) shows the temporal evolution of normalized averaged particle concentration $\langle c \rangle / c_0$, for paramagnetic manganese oxide nanoparticles. Here $\langle c \rangle$ denotes the spatially averaged particle concentration at a given time, and c_0 is the initial nanoparticle concentration. As shown in Fig. 3(c), stainless steel-430 demonstrated slightly better separation performance than stainless steel-440, followed by stainless steel-420. Overall, the difference between various sphere types is not significant. This behavior is expected because at an applied magnetic field of 1 Tesla (or equivalently $H = 0.796 \times 10^7$ [A m^{-1}]), all spheres reached their saturation magnetization M_s. Nevertheless, $M_{s,430} > M_{s,440} > M_{s,420}$, and therefore, it is expected that the magnetic field gradients around these spheres follow the same trend. On the other hand, Fig. 3(b) shows the spatio-temporal evolution of normalized concentration for diamagnetic bismuth oxide particles. Fig. 3(d) shows the corresponding temporally averaged normalized concentration of diamagnetic bismuth oxide particles. For the diamagnetic particles, the type of stainless steel sphere, and the resulting magnetization does not make a significant difference on rate of particle capture. In addition, the diamagnetic particle capture around the sphere is much smaller than those of paramagnetic particles.

Following these experiments, we performed detailed multi-physics simulations using the particle size distribution obtained from sedimentation measurements. The corresponding simulation results are shown as dashed curves in Fig. 3(c) and (d). While these simulations agree well with the experimental concentration profiles for diamagnetic Bi_2O_3 nanoparticles, they underpredict the concentration changes measured for paramagnetic Mn_2O_3. To achieve agreement with the Mn_2O_3 experiments, a larger effective particle size distribution than that obtained from sedimentation is required. Table 2 summarizes the adjusted size distributions that yield the best agreement for each stainless-steel sphere type with the corresponding simulation results

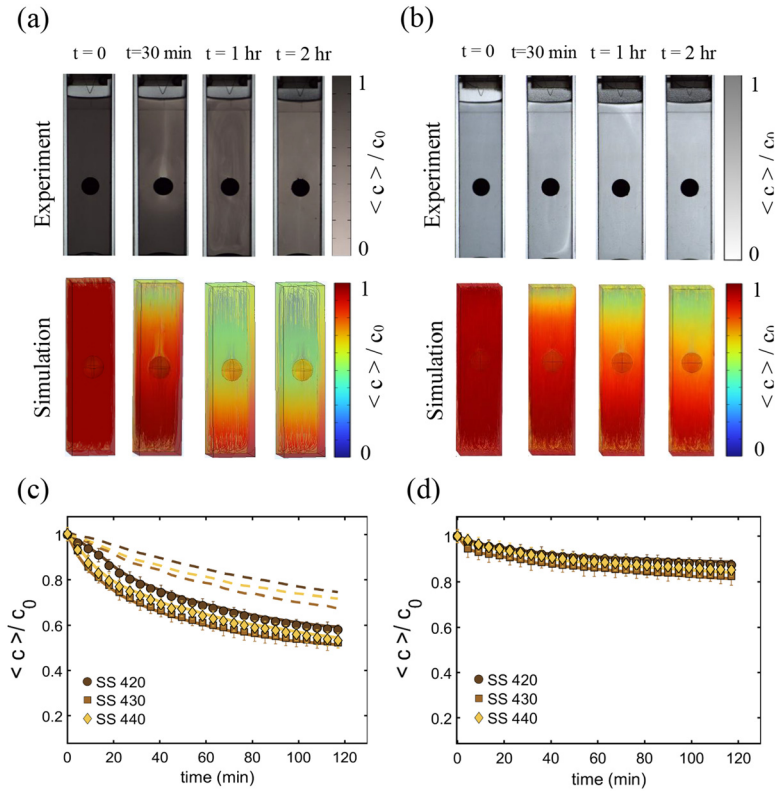

Fig. 3 The spatio-temporal evolution of (a) Mn_2O_3 and (b) Bi_2O_3 nanoparticle concentrations as measured in experiments at an initial concentration of 100 [mg L^{-1}], magnetic field $\mathbf{B}_0$ = 1 [T] and sphere diameter d = 4 mm (top row) and calculated through numerical simulations (bottom row). The temporal evolution of the normalized concentration of (c) manganese oxide and (d) bismuth oxide nanoparticles for different stainless steel types. The dashed lines correspond to simulation results obtained using the nanoparticle size provided by the vendor.

Table 2 Particle size distribution for different stainless steel simulations performed under an external magnetic field of $\mathbf{B}_0$ = 1 T and fixed concentration c_0 = 100 mg L^{-1}

	Mn_2O_3						Bi_2O_3					
SS type	ϕ_i			R_{pi} [nm]			ϕ_i			R_{pi} [nm]		
420	0.72	0.18	0.10	150	400	700	0.77	0.13	0.10	80	120	160
430	0.72	0.18	0.10	150	500	800	0.77	0.13	0.10	80	120	160
440	0.72	0.18	0.10	150	450	750	0.77	0.13	0.10	80	120	160

shown as solid curves in Fig. 3(c) and (d). The particle fractions ϕ_i reported in Table 2, and throughout the manuscript represent effective magnetic field-dependent particle size distributions, and are assumed to be fixed over time.

Several key observations emerge. First, the inferred size distribution for Mn_2O_3 shifts toward larger particle sizes, with an increased mass fraction associated with these larger aggregates compared to the no-field case (*cf.* Table SI in the SI). This trend suggests the presence of magnetic-field-induced aggregation and cluster formation among the paramagnetic nanoparticles. Second, the nanoparticle size distribution remains largely insensitive to the type of stainless-steel sphere used. The conditions under which field-induced clustering becomes significant are discussed later in the manuscript. In contrast, the fitted size distribution for diamagnetic Bi_2O_3 closely matches that obtained under no-field conditions, consistent with the absence of significant field-induced aggregation in diamagnetic nanoparticles.

4.2.2 Competition between magnetic force and effective capture area. Another important aspect of this study is the competition between the magnetic field gradients generated around the sphere and the total surface area available for particle capture. These two factors do not scale in the same manner. As the sphere size increases, the magnetic field gradient around the sphere decreases (this is clearly shown in Fig. 2(e)), which may reduce the magnetophoretic force acting on the nanoparticles. Whereas, increasing the sphere size increases the total available surface area for nanoparticle capture. Understanding which of these opposing effects dominates is critical for the rational design of sphere-based nanoparticle capture systems. To evaluate this competition, we next examine how the sphere diameter influences nanoparticle capture dynamics.

Fig. 4(a) presents the temporal evolution of averaged, normalized concentration of paramagnetic manganese oxide nanoparticles for different stainless steel sphere diameters at an imposed magnet field of 1 Tesla. The results clearly indicate that the separation dynamics are significantly enhanced with increasing sphere size, as evidenced by a greater depletion of nanoparticles from the solution cell when larger spheres are

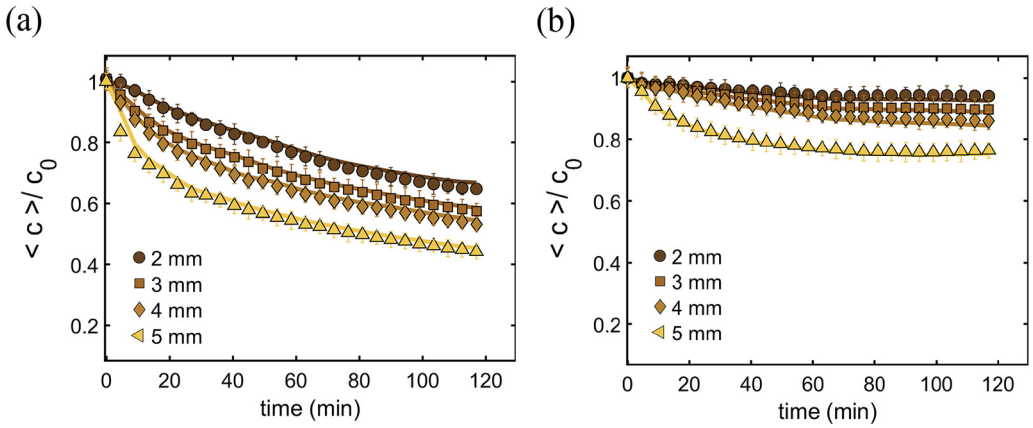

Fig. 4 The temporal evolution of normalized averaged concentration in the cuvette for (a) manganese oxide and (b) bismuth oxide nanoparticles for different stainless-steel (440) sphere diameters, at an initial concentration of 100 mg L^{-1} under a magnetic field of $\mathbf{B}_0$ = 1 T. The solid curves denote the results of numerical simulations that are best matched to the experimental results. To better understand the above experimental results on the effect of sphere size, we developed a simple scaling analysis as follows.

used (see Fig. S4 for the corresponding spatio-temporal concentration profiles). Interestingly, the capture dynamics are initially much faster for larger spheres, and at later times (around 120 min), the total Mn_2O_3 nanoparticle capture approximately doubles as the sphere diameter nearly doubles. A corresponding set of experiments was performed with diamagnetic bismuth oxide (Bi_2O_3) nanoparticles, and the results are shown in Fig. 4(b). Similar to paramagnetic particles, increasing the sphere diameter leads to a moderate enhancement in the rate of concentration depletion within the system. Diamagnetic particles preferentially accumulate near the poles of the sphere (and that is observed in our experiments), where the magnetic field is weakest.

If we consider the capture of dilute paramagnetic nanoparticles by a magnetized sphere of radius a placed in a uniform external magnetic field $\mathbf{B}_0$, the magnetophoretic force acting on a nanoparticle is given by

$$F_m = \frac{V_p \Delta\chi_v}{\mu_0}(B \cdot \nabla)B, \tag{1}$$

where μ_0 is the permeability of free space, V_p is the particle volume, and $\Delta\chi_v$ is the volume magnetic susceptibility contrast relative to the suspending fluid. On the other hand, a sphere magnetized by a uniform field behaves as a magnetic dipole with a moment[55]

$$m \sim \frac{a^3}{\mu_0}B_0. \tag{2}$$

The magnetic field outside the sphere scales as:[55]

$$B(r) \sim B_0\left(\frac{a^3}{r^3}\right) \Rightarrow B \cdot \nabla B \sim \frac{B_0^2 a^6}{r^7}. \tag{3}$$

Therefore, the magnetic force acting on a nanoparticle at distance r from the sphere center scales as:

$$F_m(r) \sim \frac{V_p \Delta\chi_v}{\mu_0}\frac{B_0^2 a^6}{r^7}. \tag{4}$$

A characteristic capture radius r_c may be defined by balancing magnetic force with competing forces. As nanoparticles approach the sphere due to the magnetic force, the thermal diffusion competes against it. At the capture radius, one can argue that these forces are equal to each other. As a result, in the limit of small Reynolds number and no particle–particle interactions, the magnetophoretic drift velocity can be obtained by scaling the magnetic force and Stokes' drag as

$$v_{mig} \sim \frac{F_m}{6\pi\eta R_p}, \tag{5}$$

where η is the fluid viscosity and R_p is the nanoparticle radius. Subsequently, at the capture zone, the diffusive flux of species could be equal to the magnetophoretic flux. Balancing magnetic drift with diffusive transport (see details of the analysis in the SI), $v_{mig} \sim D/r_c$, yields

$$r_c \sim a{B_0}^{1/3}. \tag{6}$$

Inside the capture sphere of radius r_c, the flux of nanoparticles is dominated by magnetophoretic drift, and can be approximated as:

$$\Pi \sim 4\pi {r_c}^2 c_0 v_{mig} \sim 4\pi r_c c_0 D, \tag{7}$$

where c_0 is the bulk nanoparticle concentration. Since $r_c \sim a$, the capture rate can be approximated as: $\Pi \sim c_0 Da{B_0}^{1/3}$. Based on the latter scaling, the flux of nanoparticles scales linearly with sphere size, while to a weaker degree with the imposed magnetic field. Therefore, although increasing the sphere radius (a) reduces the local magnetic field gradient, the geometric increase in the capture region dominates. Consequently, larger magnetized spheres are expected to enhance nanoparticle capture efficiency despite weaker local gradients. The latter conclusion is consistent with experiments reported in Fig. 4(a) and (b).

Although the above scaling analysis provides a useful estimate, it neglects important factors such as hydrodynamic interactions between nanoparticles and fluid, nanoparticle size

Table 3 Particle size distribution for different sphere diameter simulations performed under an external magnetic field of $\mathbf{B}_0$ = 1 T and fixed concentration c_0 = 100 mg L^{-1}

Dia.	Mn_2O_3						Bi_2O_3					
[mm]	ϕ_i			R_{pi} [nm]			ϕ_i			R_{pi} [nm]		
2	0.72	0.18	0.10	150	400	750	0.77	0.13	0.10	80	120	160
3	0.72	0.18	0.10	150	450	750	0.77	0.13	0.10	80	120	160
4	0.72	0.18	0.10	150	450	750	0.77	0.13	0.10	80	120	160
5	0.72	0.18	0.10	150	450	800	0.77	0.13	0.10	80	120	160

distributions, and assumes steady flow. To obtain a more complete understanding, we performed detailed numerical simulations to quantitatively capture these effects and provide deeper insight into the experimental results. The temporal evolution of the average particle concentration was quantitatively captured using numerical simulations, and the results are shown as continuous curves in Fig. 4(a). A closer examination of the particle size distribution that provides the best agreement between experiments and simulations reveals an additional aspect of the system not addressed in the preceding scaling analysis: namely, the potential for field-induced nanoparticle cluster formation. As summarized in Table 3, the application of a magnetic field induces a noticeable skew in the particle size distribution toward larger sizes for all spheres tested, resulting in an increased fraction of aggregates relative to the zero-field case (*cf.* Table 3 and Table SI in the SI). Notably, as the sphere diameter increases, the average particle size and fraction of larger clusters remain unchanged. These observations indicate that the enhanced magnetic capture of nanoparticles with increasing sphere diameter as reported in experiments, is not a result of field-induced clustering, but rather arises from the scaling of the total magnetic flux with sphere size (a), as discussed in the previous analysis. The mechanisms and implications of field-induced clustering will be addressed in greater detail in subsequent sections.

In terms of leading order, the above scaling analysis predicts that in addition to sphere size, the particle flux scales with the susceptibility contrast between the particles and the surrounding fluid, implying that the capture of diamagnetic particles should increase with sphere size, though to a significantly lesser extent than for paramagnetic nanoparticles. The latter is consistent with our experimental results shown in Fig. 4(b). Notably, our numerical simulations indicate that diamagnetic nanoparticles do not experience field-induced clustering under an applied magnetic field compared to the zero-field case. Therefore, the resulting enhancement in diamagnetic particle capture is associated with the increase in surface area of the sphere.

4.2.3 Initial particle concentration. According to the above scaling analysis, initial particle concentration is expected to have a significant effect on the magnetophoretic motion of nanoparticles. Fig. 5(a) and (b) show the temporal evolution of nanoparticle concentration as a function of time for both manganese oxide (a) and bismuth oxide (b) nanoparticles for an applied magnetic field of $\mathbf{B}_0$ = 1 T. The experiments clearly demonstrate that increasing the initial concentration leads to a correspondingly faster depletion of particles from the suspension. This behavior is expected: as indicated by the scaling analysis discussed above, the particle flux, and consequently the rate of concentration decay, scales linearly with the initial particle concentration. Albeit, the experimental results indicate a stronger-than-linear dependence of capture dynamics on the initial concentration of paramagnetic Mn_2O_3. For example, at 10 mg L^{-1}, the total particle capture is below 2%, whereas at c_0 = 100 mg L^{-1}, it increases to approximately 60% for Mn_2O_3.

To further evaluate these observations, multiphysics simulations of particle transport were performed under an applied magnetic field of $\mathbf{B}_0$ = 1 T. Simulations were performed and matched to the experimental results by adjusting the particle size distribution, as summarized in Table 4, and shown as continuous curves in Fig. 5(a). For the lowest concentration of 10 mg L^{-1}, the particle size distribution does not significantly change compared to the no-field particle size distribution. However, achieving this agreement at higher concentrations (50 and 100 mg L^{-1}) required either an increase in the mean particle size or an enhanced mass fraction of larger particles relative to the zero-field distribution (*cf.* Table 4 and Table SI in the SI). These findings strongly suggest that field-induced nanoparticle clustering becomes more pronounced at higher concentrations under an applied magnetic field, and that such clustering enhances the magnetic capture of paramagnetic nanoparticles. This mechanism leads to a stronger than a linear dependence of capture dynamics on the initial concentration, which is not accounted for in the scaling analysis and therefore leads to deviations from its predictions.

We next examined the behavior of diamagnetic bismuth oxide (Bi_2O_3) nanoparticles over a range of initial particle concentrations; the results are shown in Fig. 5(b). In contrast to the paramagnetic Mn_2O_3 system, the overall depletion of diamagnetic particles is substantially weaker, as expected given their much smaller negative magnetic susceptibility. Nevertheless, increasing the initial Bi_2O_3 concentration results in a faster decay of the normalized particle concentration. Experimentally, Bi_2O_3 nanoparticles are observed to accumulate primarily at the bottom of the cuvette due to gravitational settling, and to a lesser extent near the poles of the sphere, where the magnetic field is weakest. As the initial particle concentration increases, the extent of depletion correspondingly increases, and at long times the normalized concentration exhibits an approximately linear dependence on the initial concentration, consistent with the scaling analysis discussed above. To further interrogate these observations, numerical simulations were performed, and matched to the experimental results in a similar fashion to those reported for paramagnetic Mn_2O_3 nanoparticles. The corresponding results are shown as solid curves in Fig. 5(b). Achieving quantitative agreement between experiments and simulations for diamagnetic nanoparticles, only a minor increase in the volume fraction of larger particles was required (as shown Table 4 and Table SI of the SI). This behavior is expected because the diamagnetic particles of bismuth oxide should not have a tendency to undergo field-induced aggregation.

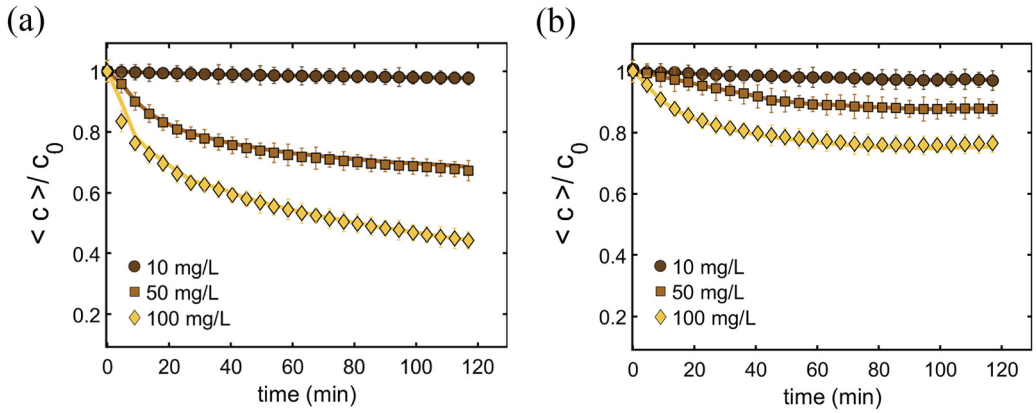

Fig. 5 Temporal evolution of normalized particle concentrations measured in experiments (symbols), and numerical simulations (solid curves) for (a) manganese oxide and (b) bismuth oxide particles at a concentration = 100 mg L^{-1}, and a magnetic field $\mathbf{B}_0$ = 1 T and a sphere diameter d = 5 mm.

Table 4 Particle size distribution for simulations performed under an external magnetic field of $\mathbf{B}_0$ = 1 T and at various initial particle concentrations

	Mn_2O_3						Bi_2O_3					
c_0 [mg L^{-1}]	ϕ_i			R_{pi} [nm]			ϕ_i			R_{pi} [nm]		
10	0.82	0.10	0.08	50	150	200	0.84	0.10	0.06	40	80	120
50	0.75	0.15	0.10	100	350	500	0.80	0.12	0.08	40	80	120
100	0.72	0.18	0.10	150	450	800	0.77	0.13	0.10	80	120	160

4.2.4 Effect of external magnetic field strength. Next we studied the effect of an imposed magnetic field on particle capture and dynamics. The temporal evolution of normalized particle concentrations is presented in Fig. 6 for paramagnetic Mn_2O_3 (a) and diamagnetic Bi_2O_3 (b) suspensions. For Mn_2O_3 nanoparticles, the normalized concentration decreases progressively with time, and the depletion rate increases as the magnetic field strength increases. This behavior is expected, and is due to the stronger magnetic force that particles experience as the imposed external magnetic field increases. Detailed numerical simulation results suggest that, again similar to previous sections, a higher likelihood of field-induced particle cluster formation. The particle size distributions obtained from the simulations at different magnetic fields, summarized in Table 5, provide further evidence of field-induced cluster formation for paramagnetic nanoparticles. For Mn_2O_3, a clear shift towards larger particle sizes is observed as the magnetic field increases. At zero magnetic field, the distribution is dominated by smaller particles, whereas at $\mathbf{B}_0$ = 0.5 T and above, the presence of larger aggregates (300–700 nm) becomes increasingly significant, accompanied by a higher mass fraction of these sizes. Fig. 6(b) shows the temporal evolution of normalized concentration for bismuth oxide nanoparticles at various imposed magnetic fields. Similar to paramagnetic Mn_2O_3, Bi_2O_3 also shows a gradual increase in particle depletion from the cell. In contrast to the paramagnetic nanoparticles, the diamagnetic Bi_2O_3 does not exhibit any significant forms of field-induced cluster formation as the magnetic field increases. The overall normalized concentration variation after two hours is summarized in Fig. 6(c) for both particle types. Fig. 6(c)

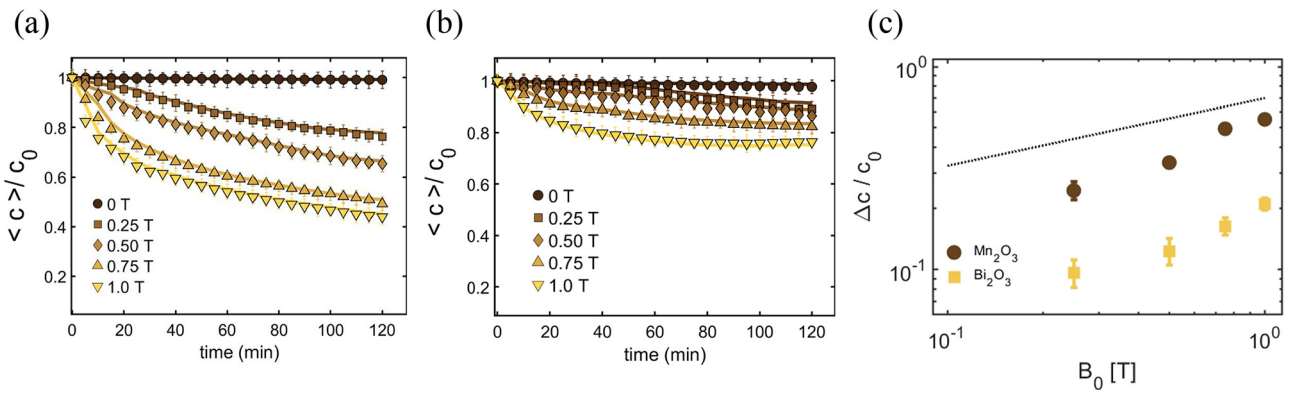

Fig. 6 Temporal evolution of normalized particle concentrations for paramagnetic Mn_2O_3 (a), and diamagnetic Bi_2O_3 (b) particles as a function of magnetic field strength ($\mathbf{B}_0$) with an initial concentration of 100 mg L^{-1} and a sphere diameter d = 5 mm. In (a) and (b) the symbols represent the experimental data, and the curves represent the simulation results that best match the experiments. (c) The normalized concentration change as a function of the imposed magnetic field after a 2 hour period for both paramagnetic (circles) and diamagnetic particles (squares). The dashed line in (c) corresponds to the prediction of the scaling analysis.

Table 5 Particle size distribution for simulations performed at a fixed concentration c_0 = 100 mg L^{-1}

Magnetic field [T]	Mn_2O_3 ϕ_i			R_{pi} [nm]			Bi_2O_3 ϕ_i			R_{pi} [nm]		
0	0.80	0.10	0.10	50	150	200	0.80	0.12	0.08	80	120	160
0.25	0.78	0.12	0.10	100	250	400	0.78	0.12	0.10	80	120	160
0.5	0.75	0.15	0.10	150	350	500	0.78	0.12	0.10	80	120	160
0.75	0.72	0.18	0.10	150	400	700	0.78	0.12	0.10	80	120	160
1	0.72	0.18	0.10	150	450	800	0.77	0.13	0.10	80	120	160

shows a steady increase in concentration change with field strength for Mn_2O_3, while Bi_2O_3 undergoes a weaker increase in concentration variations. If we consider the total volume of the suspension outside the capture zone to be the control volume (or our system), we can write a mass balance on nanoparticles as:

$$-\Pi = \frac{\mathrm{d}}{\mathrm{d}t}(cV), \tag{8}$$

where V is the system volume. Rearranging this equation and integration leads to a scaling of the particle concentration change as a function of multiple parameters:

$$\frac{c_0 - c(t)}{c_0} = \frac{\Delta c}{c_0} \sim \frac{\Pi t}{V} \Rightarrow \frac{\Delta c}{c_0} \sim \left(\frac{a\Delta\chi_v^{1/6} B_0^{1/3}}{V}\right) t \tag{9}$$

The scaling prediction with respect to the applied magnetic field is shown as a dashed line in Fig. 6(c), and it underpredicts the experimental results for paramagnetic Mn_2O_3 nanoparticles. Experimentally, we find that $\Delta c/c_0 \sim B_0^{0.65}$ for Mn_2O_3, whereas for diamagnetic Bi_2O_3, $\Delta c/c_0 \sim$ **B**00.51. This discrepancy likely arises from mechanisms not captured in the simple scaling analysis, including field-induced clustering of paramagnetic nanoparticles and magnetically driven convective flows present in both paramagnetic and diamagnetic systems. We will revisit these flow features later.

4.2.5 Magnetic susceptibility. Finally, we return to the impact of nanoparticle magnetic susceptibility. Fig. 7(a) shows the temporal evolution of particle concentration for various nanoparticle types under a magnetic field $\mathbf{B}_0$ = 1 T, c_0 = 100 mg L^{-1} and the sphere diameter d = 5 mm. Paramagnetic particles (manganese, cobalt, iron, copper) exhibit a continuous decrease in bulk concentration over time, indicating effective particle capture around the magnetized sphere. Among the diamagnetic materials, bismuth oxide exhibits a notable change in concentration, indicating measurable repulsion from the high-gradient region, whereas zinc oxide shows only a weak response due to its comparatively small magnetic susceptibility. Fig. 7(b) presents the normalized change in particle concentration, $\Delta c/c_0$, after two hours as a function of magnetic susceptibility $\Delta\chi_v$ for all nanoparticles considered in this study. For paramagnetic nanoparticles, $\Delta c/c_0$ increases strongly with magnetic susceptibility, with manganese oxide exhibiting the largest concentration change, followed by iron oxide, while cobalt oxide and copper oxide show comparatively weaker magnetophoretic capture. The dashed line in Fig. 7(b) represents the scaling predicted by eqn (9). Although the scaling captures the general trend at low magnetic susceptibility, it underpredicts the experimentally observed dependence at higher susceptibilities. To elucidate the discrepancy between the experiments and the scaling analysis, we performed detailed numerical simulations of particle transport. The best agreement with experiments is shown as solid curves in Fig. 7(a). The corresponding particle size distributions, both in the absence of a magnetic field and under an applied field of 1 T, are summarized in Table 6. The results indicate that paramagnetic particles form larger clusters in the presence of a magnetic field, with iron and copper oxides reaching effective sizes exceeding 500 nm. This growth substantially enhances the magnetic force acting on the clusters, thereby accelerating their magnetophoretic capture to the sphere. Such field-induced clustering likely accounts for the discrepancy between the

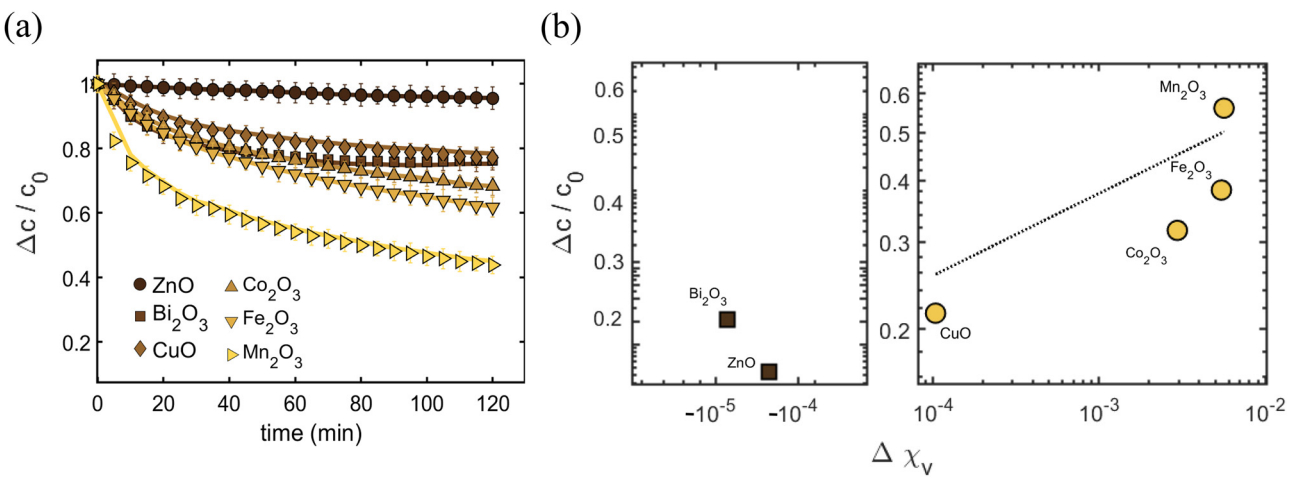

Fig. 7 (a) Temporal evolution of normalized particle concentrations for all the paramagnetic and diamagnetic nanoparticles considered in this study with an initial concentration of 100 mg L^{-1}, $\mathbf{B}_0$ = 1 T and a sphere diameter d = 5 mm. Here, the symbols represent the experimental data, and the solid curves represent the simulation results that best match the experiments. (b) Normalized change in concentration as a function of magnetic susceptibility $\Delta\chi_v$.

Table 6 Particle size distributions used in simulations under external magnetic fields of $\mathbf{B}_0$ = 0 T and $\mathbf{B}_0$ = 1 T for evaluating the effect of magnetic susceptibility

	B_0 = 0 T						B_0 = 1 T					
Material	ϕ_i			R_{pi} [nm]			ϕ_i			R_{pi} [nm]		
ZnO	0.84	0.10	0.06	18	36	54	0.82	0.10	0.08	18	36	54
CuO	0.84	0.10	0.06	40	80	120	0.76	0.14	0.10	80	160	400
Co_2O_3	0.82	0.10	0.08	50	100	150	0.74	0.14	0.12	100	200	450
Fe_2O_3	0.82	0.10	0.08	60	90	150	0.74	0.14	0.12	120	270	630

scaling predictions and the experimental trends observed in Fig. 7(b). In contrast, diamagnetic zinc oxide shows no evidence of field-induced clustering, consistent with its comparatively weak response.

4.3 Field-induced cluster formation

Our numerical simulations suggest that the paramagnetic nanoparticles may undergo field-induced cluster formation near the sphere under certain operating conditions such as initial concentration, applied magnetic field, and particle magnetic susceptibility. It has been well established in previous literature that magnetic particles can self-assemble and undergo field-induced cluster formation.[56,57] Prior literature reports have advanced theoretical and experimental aspects and illustrated that under a uniform magnetic field, two dimensionless quantities can describe the threshold for the onset of field-induced cluster formation.[58,59] These dimensionless numbers include the magnetic coupling parameter Γ and the aggregation parameter N^*. The coupling parameter Γ expresses the competition between magnetic dipolar energy and thermal agitation. Under an externally imposed magnetic field, magnetic nanoparticles develop induced magnetic dipoles and, through dipole–dipole interactions, experience attractive forces that promote field-induced aggregation and cluster formation. The strength of these interactions is commonly characterized by the dimensionless interaction parameter Γ, defined as:[31]

$$\Gamma = \frac{\pi \Delta\chi^2 B^2 R_p^3}{9\mu_0 k_B T}. \quad (10)$$

The aggregation parameter N^* reflects the role of particle concentration in promoting collective behavior and is expressed as:

$$N^* = \sqrt{\phi_0 e^{\Gamma-1}}. \quad (11)$$

Here, ϕ_0 is the volume fraction of the nanoparticles in the solution. It has been demonstrated through both experiments and theoretical studies that under a uniform magnetic field, field-induced cluster formation occurs for conditions that satisfy $\Gamma > 1$ and $N^* > 1$. Although in our experiments the magnetic field around the sphere is highly non-uniform, these dimensionless numbers offer a reasonable first-order assessment of field-induced cluster formation.

Fig. 8 presents a series of phase diagrams showing the variation of the coupling parameter Γ (a) and (c) and the aggregation parameter N^* (b) and (d) as functions of particle radius (R_p) and applied magnetic field strength ($\mathbf{B}_0$). Panels (a) and (b) correspond to various initial concentrations of Mn_2O_3 nanoparticles, whereas panels (c) and (d) represent other nanoparticles when magnetic susceptibility is varied. The solid curves denote the threshold conditions $\Gamma = 1$ and $N^* = 1$, which together define the necessary criterion for the onset of field-induced cluster formation. Regions beyond these threshold curves correspond to parameter combinations for which clustering is expected, while clustering is not anticipated below the thresholds.

As shown in Fig. 8(a) and (b), decreasing the initial concentration of Mn_2O_3 nanoparticles shifts the onset of cluster formation toward larger particle radii and higher magnetic field strengths. At an initial concentration of 10 mg L^{-1}, the predicted thresholds for clustering occur at particle sizes and magnetic fields that lie well beyond the experimental conditions used in this study. Consequently, field-induced cluster formation is not expected under these conditions, consistent with the magnetophoresis experiments and numerical simulations discussed above in Fig. 5. Conversely, at higher initial concentrations, the predicted onset of field-induced clustering falls within the experimentally accessible ranges of particle size and magnetic field strength. Under these conditions, the analysis predicts the formation of magnetic-field-induced particle clusters, in agreement with the experimental observations and numerical simulation results reported earlier in Fig. 5.

While the above discussion provides a valuable theoretical criterion for predicting the onset of clustering as a function of initial concentrations, our experiments with Mn_2O_3, at an initial concentration of 100 mg L^{-1} and various imposed magnetic fields ($\mathbf{B}_0$; as shown in Fig. 6) suggest that field-induced cluster formation exists at a considerably lower magnetic field ($\mathbf{B}_0 \sim 0.25$ T) than what this framework predicts (which is for $\mathbf{B}_0 > 0.75$ T). The model that relies on the thresholds for Γ–N^* assumes a uniform magnetic field. However, in this study, the magnetic field around the magnetized sphere is extremely non-uniform. The non-uniform magnetic field may (i) directly increase magnetophoretic drift and hence collision frequency between particles, and/or (ii) induce weak but finite fluid flows through particle–fluid coupling. The latter effect will be discussed in detail below. Eventually, these two effects are expected to further enhance transport and association of particles towards cluster formation.

Fig. 8(c) and (d) illustrate the onset of field-induced clustering for nanoparticles with varying magnetic susceptibilities at an initial concentration of 100 mg L^{-1}. Based on these two dimensionless parameters (Γ–N^*), increasing magnetic susceptibility promotes cluster formation at smaller particle sizes and/or lower applied magnetic fields. Accordingly, for CuO, clustering is not expected within the range of particle sizes and magnetic fields considered in Fig. 8 (for this reason, the curve associated with this nanoparticle cannot be seen in the range of parameters reported in Fig. 8(c) and (d)). However,

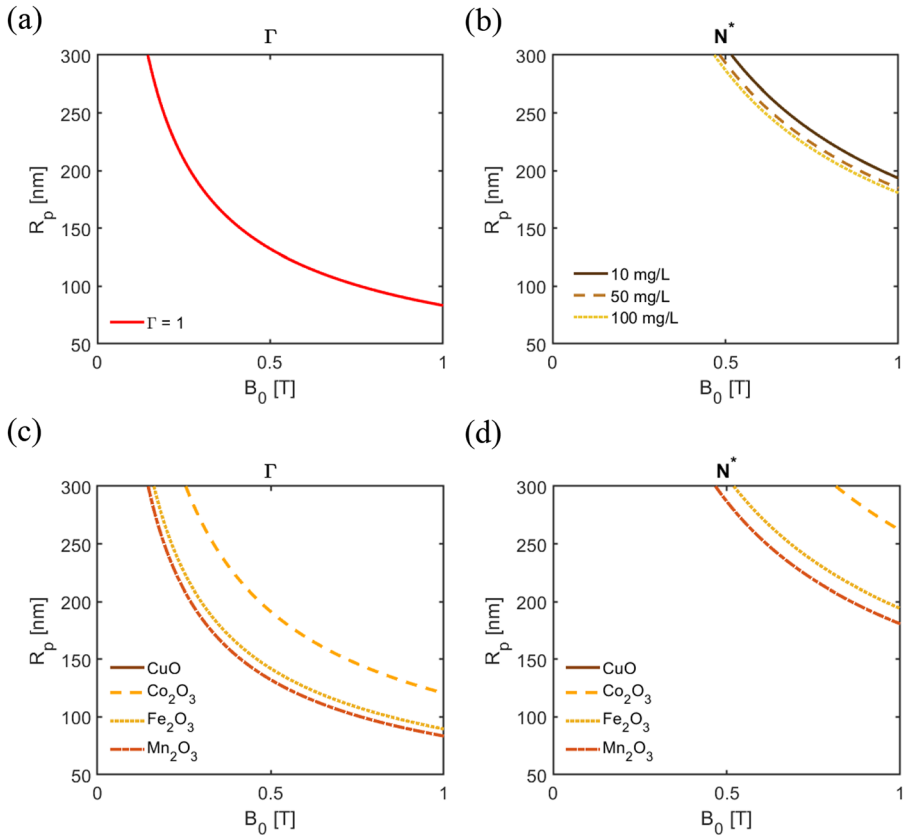

Fig. 8 Plot of Γ (a) and N^* (b) are presented as functions of particle size R_p and magnetic field $\mathbf{B}_0$ for Mn_2O_3 nanoparticles at different initial concentrations (c_0 = 10, 50, and 100 mg L^{-1}). (c) and (d) denote Γ and N^* for nanoparticles with different magnetic susceptibilities and an initial concentration of 100 mg L^{-1}. The curves highlight the points where Γ = 1 and N^* = 1. Note that within the range of particle sizes and applied magnetic fields, CuO is not expected to reach the thresholds of Γ = 1 or N^* = 1.

the magnetophoretic experiments and simulations in Fig. 7(a) indicate that even this weakly paramagnetic nanoparticle exhibits modest field-induced clustering at $\mathbf{B}_0$ = 1 T. For the remaining nanoparticles, the dimensionless parameters exceed unity over the relevant range of particle sizes and magnetic fields, suggesting that clustering should occur under an applied field of 1 T according to the Γ–N^* framework, and that is consistent with our magnetophoresis experiments and simulations on those nanoparticles. The discrepancy observed for CuO may arise from the non-uniformity of the magnetic field, as discussed above.

4.4 Field-induced convective flows

An important aspect of this study that has not yet been discussed in detail is the role of field-induced convective flows. These flows are expected to arise from the coupling between magnetophoretic nanoparticle motion and the surrounding fluid. As nanoparticles migrate under the influence of a non-uniform magnetic field, they transfer momentum to the fluid, which in turn should generate convective flows. In this section, we quantify this effect and its role in the transport of nanoparticles. Fig. 9(a) shows the computed fluid velocity vectors and velocity magnitude around a sphere for a suspension containing 100 mg L^{-1} Mn_2O_3 nanoparticles, subjected to an imposed magnetic field B_0 = 1 T and a sphere diameter of 5 mm. Shortly after the onset of flow, the fluid velocity increases rapidly, reaching a maximum before gradually decreasing and approaching a steady value. To quantify this temporal behavior, Fig. 9(b) presents the temporal evolution of the maximum fluid velocity $u_{f,max}$ within the computational domain at the lowest and highest magnetic field gradients used in this study that correspond to $\mathbf{B}_0$ = 0.25 T and $\mathbf{B}_0$ = 1.0 T. At the lower field gradient of 123 T^2 m^{-1}, the induced flow increases rapidly to a maximum velocity of $\approx$0.1 mm s^{-1} before gradually decaying, whereas at the higher field gradient of 630 T^2 m^{-1} the maximum velocity exceeds $\approx$0.3 mm s^{-1} with a similar transient behavior. For both cases, the fluid velocity decays quickly and approaches a nearly constant value at longer times. This overshoot can be rationalized by considering the evolution of particle concentration near the sphere surface with a high field gradient as follows. At t = 0 for both cases, the suspension is spatially uniform, resulting in negligible driving forces for fluid motion. As particles undergo magnetophoretic motion and are captured by the sphere, concentration gradients emerge, which in turn initiate magnetically driven convection. The establishment of a concentration gradient enhances the local driving force, producing a maximum in $u_{f,max}$. With continued depletion, the overall concentration of particles in the domain

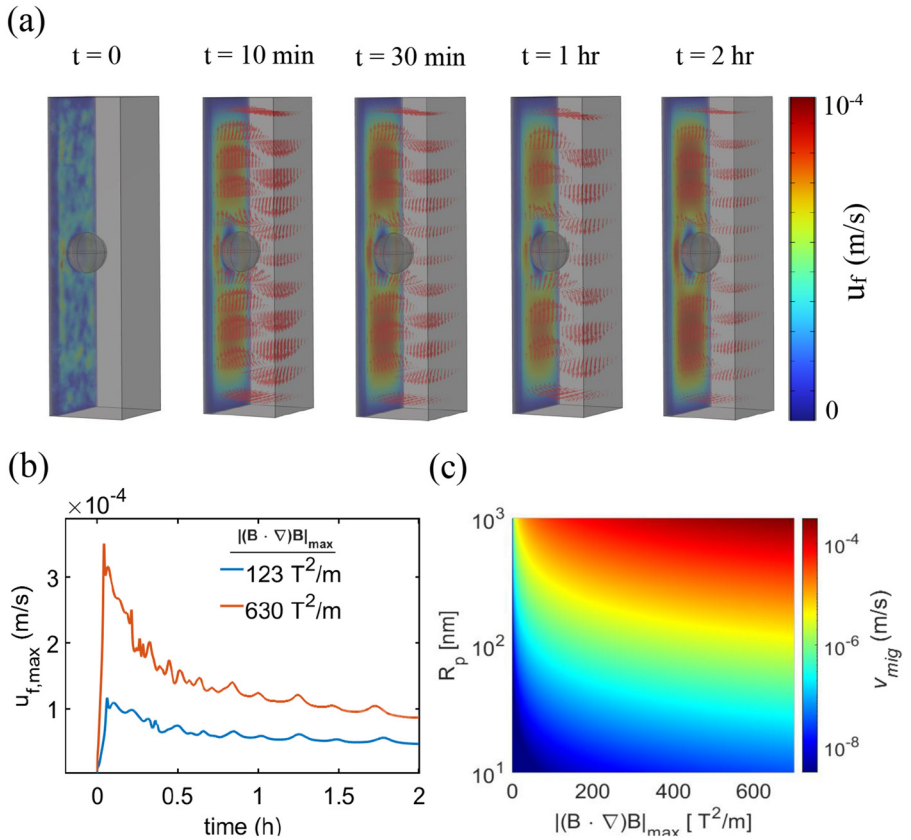

Fig. 9 (a) Spatio-temporal evolution of velocity vectors and velocity magnitude for paramagnetic Mn_2O_3 nanoparticles at c_0 = 100 mg L^{-1} and $\mathbf{B}_0$ = 1 T. (b) Temporal evolution of the maximum fluid velocity at the lowest and highest magnetic field strength used in this study. (c) Magnetophoretic particle velocity as a function of particle size and magnetic field gradient calculated for paramagnetic Mn_2O_3 nanoparticles at c_0 = 100 mg L^{-1}.

decreases, and the concentration gradients weaken. The latter leads to a gradual reduction in the induced velocity. Fig. 9(b) presents the calculated magnetophoretic particle velocity, v_{mig}, as a function of particle radius, R_p and magnetic field gradients. The v_{mig} increases monotonically with both R_p and $(\mathbf{B}\cdot\nabla)\mathbf{B}$, with larger particles experiencing orders-of-magnitude higher velocities compared to smaller counterparts. Notably, the maximum fluid velocities $u_{f,max}$ obtained from the fully coupled simulations significantly exceed the corresponding magnetophoretic particle velocities of the particle or v_{mig} under otherwise similar particle and magnetic field conditions. This disparity provides strong evidence for the emergence of field-induced convective flows arising from momentum transfer between migrating nanoparticles and the surrounding fluid. Such flows are expected to enhance particle transport and promote more efficient separation and capture. To verify this, we performed additional simulations in which fluid flow was neglected (not solved for, and it is assumed that $u_f = 0$) and only particle transport was considered; the results are shown in Fig. S5 of the SI. The comparison clearly demonstrates that fluid–particle interactions significantly enhance the magnetophoretic capture of paramagnetic nanoparticles.

To further evaluate the formation of these induced convective flows and by drawing an analogy between natural convection and magnetic field-induced convective flows, a dimensionless magnetic Grashof number appears. The magnetic Grashof number Gr_m characterizes the relative importance of the magnetically induced body forces and viscous forces in the system, and can be defined as:[42]

$$Gr_m = \frac{\rho \Delta\chi_m |c_s - c_\infty| L^3 |(\mathbf{B}\cdot\nabla)\mathbf{B}|}{M_i(1+\chi_{v,f})\mu_0\eta^2}, \quad (12)$$

Here, ρ is the density of the magnetic particles, taken as Mn_2O_3 = 5.03 g cm^{-3}, Fe_2O_3 = 5.24 g cm^{-3}, Co_2O_3 = 5.18 g cm^{-3}, and CuO = 6.31 g cm^{-3}, $\Delta\chi_m$ is the molar magnetic susceptibility of the nanoparticles, c_0 represents the concentration of the particles and c_∞ is the concentration of the surrounding medium. The parameter L is the critical length, which is the cuvette width, and M_i is the molar mass of nanoparticle i, and $\chi_{v,f}$ (-9.07×10^{-6}) is the volume magnetic susceptibility of the surrounding fluid. The permeability of free space is given by μ_0, and $\eta = 1 \times 10^{-3}$ Pa s is the dynamic viscosity of the fluid.

Fig. 10(a) presents the heat map of the magnetic Grashof number Gr_m as a function of initial concentration and magnetic field gradients for paramagnetic Mn_2O_3 nanoparticles. Beginning with Mn_2O_3 nanoparticles and an initial concentration of 10 mg L^{-1}, at very low values of $(\mathbf{B}\cdot\nabla)\mathbf{B}$ up to 600 T^2 m^{-1}, Gr_m remains less than unity, indicating that the magnetically driven fluid motion is too weak. As the initial

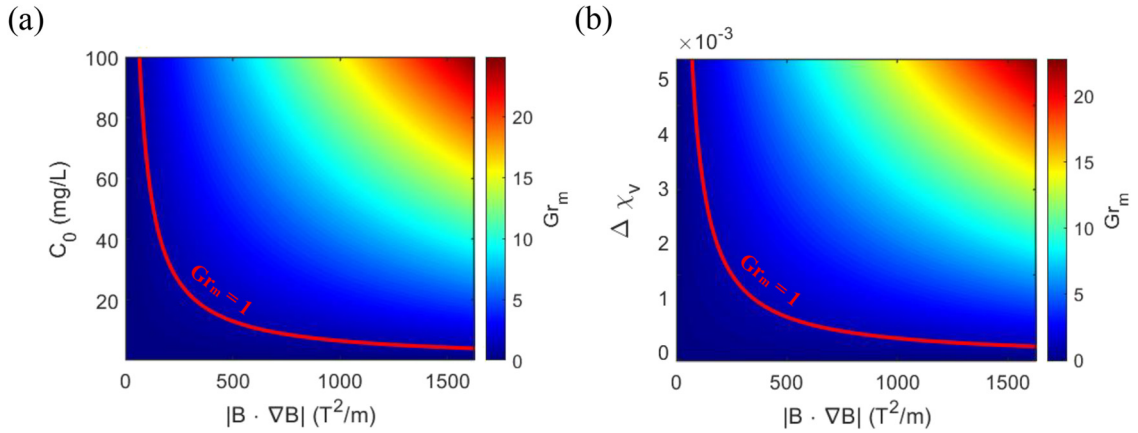

Fig. 10 (a) Map of magnetic Grashof number as a function of initial concentration and field gradients for Mn_2O_3 nanoparticles at c_0 = 100 mg L^{-1}. (b) Magnetic Grashof number as a function of magnetic field gradient and magnetic susceptibility $\Delta\chi_v$.

concentration of Mn_2O_3 nanoparticles increases, especially for 50 and 100 mg L^{-1}, it is expected that field-induced convective flows will exist for $(\mathbf{B}\cdot\nabla)\mathbf{B} > 100$–$200$ T^2 m^{-1} values. Indeed, this is consistent with our experiments that clearly show the formation of field-induced convective flows (see Movie S1 in the SI).

Fig. 10(b) shows the plot of magnetic Grashof number as a function of magnetic susceptibility and field gradients for an initial particle concentration of 100 mg L^{-1}. Based on these calculations, for paramagnetic Mn_2O_3 nanoparticles with $\Delta\chi_v = 5.6 \times 10^{-3}$, it is expected that field-induced convective flows will be present for $|\mathbf{B}\cdot\nabla\mathbf{B}| > 200$ T^2 m^{-1}, which is consistent with our experiments showing clear convective flows at higher field gradients. As the magnetic susceptibility of the nanoparticle decreases, it is expected that the onset of secondary flows will shift to higher field gradients. Under the conditions corresponding to Fig. 7(a), where $|\mathbf{B}\cdot\nabla\mathbf{B}|_{max} \approx 630$ T^2 m^{-1}, only Fe_2O_3 and Co_2O_3 are expected to exhibit field-induced convective flows. This prediction is consistent with our magnetophoresis experiments, which show clear evidence of such flows for Fe_2O_3 and Co_2O_3, but minimal response in the case of CuO (see Fig. S6 in the SI).

5 Summary and conclusions

In this study, we investigated the magnetophoretic transport and capture of nanoparticles over a broad range of magnetic susceptibilities (*e.g.*, Bi_2O_3, ZnO, CuO, Co_2O_3, Fe_2O_3, and Mn_2O_3), initial particle concentration (10–100 mg L^{-1}), imposed magnetic field (0–1 T), and magnetic field gradients (0–1500 T^2 m^{-1}) through a combination of experiments, scaling analysis, and multiphysics simulations. The results reveal that nanoparticle capture in non-uniform magnetic fields is governed by a complex interplay of magnetic forces, particle–particle interactions, and fluid–particle coupling.

For paramagnetic nanoparticles, enhanced capture is driven by magnetic-field-induced clustering, which increases effective particle size and amplifies magnetic forces. The extent of clustering grows with magnetic susceptibility, field strength, and initial concentration, leading to a strongly nonlinear dependence of magnetophoretic dynamics. In contrast, diamagnetic nanoparticles show negligible clustering and largely follow scaling predictions.

The onset of field-clustering is reasonably described by the Γ–N^* framework, although deviations arise due to the highly non-uniform magnetic field used in this study. This highly non-uniform magnetic field around the sphere promotes aggregation at lower field strengths. In addition, simulations reveal the presence of field-induced convective flows arising from particle–fluid momentum transfer. These flows significantly enhance transport and capture, as confirmed by comparisons with simulations that neglect fluid motion.

Finally, increasing sphere size enhances capture efficiency despite weaker local field gradients due to the expansion of the effective capture region. Overall, the results demonstrate that magnetophoretic capture of nanoparticles is governed by coupled effects of clustering and fluid motion, which highlight the limitations of classical scaling and provide guidance for the design of magnetic separation systems. The present study focuses on magnetized spherical geometry, however, alternative magnetic geometries capable of generating stronger localized magnetic-field gradients, such as sharp-edge collectors, corners, or optimized multi-collector configurations, may further enhance clustering, convective transport, and nanoparticle capture. Investigation of such geometries represents an important direction for future studies.

Conflicts of interest

There are no conflicts to declare.

Data availability

The data that support the findings of this study are available from the corresponding author upon reasonable request. The supplementary information (SI) includes the analytical model

for magnetic field distribution around a sphere, calibration curves for nanoparticle concentration measurements, governing equations for the multiphysics model, particle sedimentation experiments and corresponding numerical simulations, particle size distributions obtained from dynamic light scattering (DLS), additional details of the scaling analysis, magnetic separation simulations without hydrodynamic interactions, and additional experimental results for cobalt oxide, iron oxide, copper oxide, and zinc oxide nanoparticles. See DOI: https://doi.org/10.1039/d6sm00260a.

The data are available upon request.

Acknowledgements

This work was performed at the National High Magnetic Field Laboratory, which is supported by the National Science Foundation Cooperative Agreement No. DMR-1644779 and the State of Florida. This work was supported by the Center for Rare Earths, Critical Minerals, and Industrial Byproducts, through funding provided by the State of Florida. HM acknowledges National Science Foundation support through award CET 2343151. The authors gratefully acknowledge Dr. Ralm Ricarte and his graduate student, Dana Ezzeddine, for their assistance with the dynamic light scattering (DLS) measurements.

References

1 S. Li, M. Wang, Z. Zhu, Q. Wang, X. Zhang, H. Song and D. Cang, *Sep. Purif. Technol.*, 2012, **84**, 56–62.
2 D. Kelland, *IEEE Trans. Magn.*, 1973, **9**, 307–310.
3 S. S. Leong, S. P. Yeap and J. Lim, *Interface Focus*, 2016, **6**, 20160048.
4 J.-Y. Tseng, C.-C. Chang, C.-W. Tu, M.-H. Yuan, C.-Y. Chang, C.-F. Chang, Y.-H. Chen, J.-L. Shie, D.-R. Ji and B.-L. Liu, *et al.*, *Processes*, 2023, **11**, 965.
5 J. A. Ritter, A. D. Ebner, K. D. Daniel and K. L. Stewart, *J. Magn. Magn. Mater.*, 2004, **280**, 184–201.
6 V. Rizos, E. Righetti and A. Kassab, *Energy Rep.*, 2024, **12**, 1673–1682.
7 Z. Cherkezova-Zheleva, M. Burada, A. E. Sobetkii, D. Paneva, S. A. Fironda and R.-R. Piticescu, *Metals*, 2024, **14**, 658.
8 D. Teng, J. Wu, Q. Ma, W. Wang, G. Zhou, G. Fan, Y. Cao and P. Li, *ACS Omega*, 2024, **10**, 76–92.
9 F. Liu, C. Peng, A. Porvali, Z. Wang, B. P. Wilson and M. Lundstrom, *ACS Sustainable Chem. Eng.*, 2019, **7**, 16103–16111.
10 F. Deng, H. Olvera-Vargas, M. Zhou, S. Qiu, I. Sirés and E. Brillas, *Chem. Rev.*, 2023, **123**, 4635–4662.
11 G. Zante, C. E. Elgar, J. M. Hartley, R. Mukherjee, J. Kettle, L. E. Horsfall, A. Walton, G. D. Harper and A. P. Abbott, *RSC Sustainability*, 2024, **2**, 320–347.
12 A. Akthakul, A. I. Hochbaum, F. Stellacci and A. M. Mayes, *Adv. Mater.*, 2005, **17**, 532–535.
13 Y. A. Kahnouji, E. Mosaddegh and M. A. Bolorizadeh, *Mater. Sci. Eng., C*, 2019, **103**, 109817.
14 S. Shrestha, B. Wang and P. Dutta, *Adv. Colloid Interface Sci.*, 2020, **279**, 102162.
15 B. Lake, T. Siegrist, T. E. Albrecht, H. Mohammadigoushki, M. Humayun and J. Ali, *Ind. Eng. Chem. Res.*, 2025, **64**, 19781–19796.
16 Z. Hu, D. Lu, X. Zheng, Y. Wang, Z. Xue and S. Xu, *Powder Technol.*, 2023, **421**, 118435.
17 W. Ge, A. Encinas, E. Araujo and S. Song, *Results Phys.*, 2017, **7**, 4278–4286.
18 J. Svoboda, *Magnetic techniques for the treatment of materials*, Springer Science & Business Media, 2004.
19 C. T. Yavuz, J. Mayo, W. W. Yu, A. Prakash, J. C. Falkner, S. Yean, L. Cong, H. J. Shipley, A. Kan and M. Tomson, *et al.*, *Science*, 2006, **314**, 964–967.
20 L. Chen, Y. Wu, N. T. H. Nhung, C. He, H. Chen, G. Dodbiba, A. Otsuki and T. Fujita, *Metals*, 2023, **13**, 241.
21 J. Watson, *IEEE Trans. Magn.*, 1975, **11**, 1597–1599.
22 J. H. Watson, *J. Appl. Phys.*, 1973, **44**, 4209–4213.
23 M. Iranmanesh and J. Hulliger, *Chem. Soc. Rev.*, 2017, **46**, 5925–5934.
24 A. Ditsch, S. Lindenmann, P. E. Laibinis, D. I. Wang and T. A. Hatton, *Ind. Eng. Chem. Res.*, 2005, **44**, 6824–6836.
25 G. D. Moeser, K. A. Roach, W. H. Green, T. Alan Hatton and P. E. Laibinis, *AIChE J.*, 2004, **50**, 2835–2848.
26 J. Svoboda, *Magnetic techniques for the treatment of materials*, Springer Science & Business Media, 2004.
27 S. S. Leong, Z. Ahmad, S. C. Low, J. Camacho, J. Faraudo and J. Lim, *Langmuir*, 2020, **36**, 8033–8055.
28 S. S. Leong, Z. Ahmad and J. Lim, *Soft Matter*, 2015, **11**, 6968–6980.
29 J. Lim, S. P. Yeap and S. C. Low, *Sep. Purif. Technol.*, 2014, **123**, 171–174.
30 V. Schaller, U. Kräling, C. Rusu, K. Petersson, J. Wipenmyr, A. Krozer, G. Wahnström, A. Sanz-Velasco, P. Enoksson and C. Johansson, *J. Appl. Phys.*, 2008, **104**, 093918.
31 G. De Las Cuevas, J. Faraudo and J. Camacho, *J. Phys. Chem. C*, 2008, **112**, 945–950.
32 M. Klokkenburg, R. P. Dullens, W. K. Kegel, B. H. Erné and A. P. Philipse, *Phys. Rev. Lett.*, 2006, **96**, 037203.
33 M. Klokkenburg, B. H. Erné, J. D. Meeldijk, A. Wiedenmann, F. A. V. Petukhov, R. P. Dullens and A. P. Philipse, *Phys. Rev. Lett.*, 2006, **97**, 185702.
34 V. Socoliuc, L. Vékás and R. Turcu, *Soft Matter*, 2013, **9**, 3098–3105.
35 J. M. Laskar, J. Philip and B. Raj, *Phys. Rev. E: Stat., Nonlinear, Soft Matter Phys.*, 2010, **82**, 021402.
36 G. P. Gajula, M. T. Neves-Petersen and S. B. Petersen, *Appl. Phys. Lett.*, 2010, **97**, 103103.
37 H. Ezzaier, J. Alves Marins, I. Razvin, M. Abbas, A. Ben Haj Amara, A. Zubarev and P. Kuzhir, *J. Chem. Phys.*, 2017, **146**, 114902.
38 J. S. Andreu, J. Camacho and J. Faraudo, *Soft Matter*, 2011, **7**, 2336–2339.
39 J. Faraudo, J. S. Andreu and J. Camacho, *Soft Matter*, 2013, **9**, 6654–6664.

40 A. Isldar, E. D. van Hullebusch, M. Lenz, G. Du Laing, A. Marra, A. Cesaro, S. Panda, A. Akcil, M. A. Kucuker and K. Kuchta, *J. Hazard. Mater.*, 2019, **362**, 467–481.
41 K. H. Chan, J. Anawati, M. Malik and G. Azimi, *ACS Sustainable Chem. Eng.*, 2021, **9**, 4398–4410.
42 P. Rassolov, J. Ali, T. Siegrist, M. Humayun and H. Mohammadigoushki, *Phys. Rev. Fluids*, 2025, **10**, 073701.
43 M. B. Khan, P. Rassolov, J. Ali, T. Siegrist, M. Humayun and H. Mohammadigoushki, *J. Chem. Phys.*, 2025, **163**, 024903.
44 S. Arajs, C. A. Moyer, R. Aidun and E. Matijevic, *J. Appl. Phys.*, 1985, **57**, 4286–4288.
45 M. Haque, R. Aidun, C. Moyer and S. Arajs, *J. Appl. Phys.*, 1988, **63**, 3239–3240.
46 F. Friedlaender, R. Gerber, H.-P. Henkel and R. Birss, *IEEE Trans. Magn.*, 2003, **17**, 2804–2806.
47 L. A. Romo, A. López-Fernández, I. Garca-Daz, P. Fernández, A. Urbieta and F. A. López, *RSC Adv.*, 2018, **8**, 33496–33505.
48 S. Xu, Y. Li and X. Yan, *Sep. Purif. Technol.*, 2025, **378**, 134721.
49 D. R. Lide, *CRC handbook of chemistry and physics*, CRC Press, 2004, vol. 85.
50 P. Bouguer, *Essai d'optique sur la gradation de la lumière*, Claude Jombert, 1729.
51 A. Beer, *Ann. Phys.*, 1852, **162**, 78–88.
52 F. Zuo, *Eur. J. Phys.*, 2024, **45**, 065204.
53 M. Maiorov and A. Tsebers, *Magnetohydrodynamics*, 1979, **15**, 130–134.
54 M. Maiorov and A. Cebers, *Magnetohydrodynamics*, 1983, **19**, 376–380.
55 J. D. Jackson, *Classical electrodynamics*, John Wiley & Sons, 2021.
56 E. W. Chuan Lim and R. Feng, *J. Chem. Phys.*, 2012, **136**, 124109.
57 P. J. Vikesland, R. Rebodos, J. Bottero, J. Rose and A. Masion, *Environ. Sci.: Nano*, 2016, **3**, 567–577.
58 C. Tsouris and T. Scott, *J. Colloid Interface Sci.*, 1995, **171**, 319–330.
59 J. Faraudo, J. S. Andreu, C. Calero and J. Camacho, *Adv. Funct. Mater.*, 2016, **26**, 3837–3858.